Regular Article – Atomic and Molecular Collisions

Combined experimental and theoretical study on the elastic electron scattering cross sections of ethanol

Mareike Dinger[1,2,a] , Yeunsoo Park[3], Philine Hepperle[1,4], and Woon Yong Baek[1]

[1] Physikalisch-Technische Bundesanstalt (PTB), Bundesallee 100, 38116 Brunswick, Germany
[2] Ruprecht-Karls-Universität Heidelberg, Grabengasse 1, 69117 Heidelberg, Germany
[3] Institute of Plasma Technology, Korea Institute of Fusion Energy, 37 Dongjangsan- Ro, Gunsan, Jeollabuk-Do 54004, Republic of Korea
[4] Institute of Radioecology and Radiation Protection, Leibniz University Hannover, Herrenhäuserstraße 2, 30419 Hannover, Germany

Abstract. Combined theoretical and experimental studies on the elastic scattering of electrons on ethanol were performed in the energy range of 30–800 eV. The differential elastic electron scattering cross sections (DCS) of ethanol were measured for scattering angles of 30° to 150° using the relative flow technique and nitrogen (N_2) as the reference gas. From these experimental DCS, integral elastic and momentum transfer cross sections were estimated. The comparison of the experimental results from the present work to those of other groups showed good agreement within the experimental uncertainty. In addition to the experimental determination, the DCS of ethanol were calculated by applying the independent atomic model with screening-corrected additivity rule and the modified independent atomic model. These theoretical calculations reproduced the experimental data well within the experimental uncertainty, with agreement better at high electron energies as was expected.

1 Introduction

Electron interaction cross sections of molecules play an important role in many scientific fields, including radiation dosimetry, atmospheric physics, and plasma diagnostics. Low-energy electrons are released in large amounts by any type of ionizing radiation that penetrates matter, and they are responsible for most radiation damage incurred by a medium. In current radiation therapy, treatment planning is generally based on the absorbed dose to water. Here, it is assumed that the human body consists of water of different electron densities. Dose to water, however, does not describe with sufficient accuracy the dose distribution in those areas of a patient's body where strong tissue inhomogeneities exist. Therefore, it is increasingly recommended to use dose to tissue instead of dose to water in dose delivery planning [1].

To do so, precise electron interaction cross sections of human tissue are needed in order to calculate the local distribution of a biologically effective dose within a patient undergoing radiotherapy. With the aim of providing a comprehensive database for radiation transport calculations in real tissue, a project has been launched by the present group to measure electron interaction cross sections of molecules carrying functional groups contained in tissue building blocks. The experiments are accompanied by theoretical research to quantify the contribution of the functional groups to the electron interaction cross sections of tissue components. One basic functional group of biomolecules is the hydroxyl group, which is carried by the ethanol molecule. For this reason, the project began with the determination of the electron interaction cross sections (i.e., singly differential elastic scattering and doubly differential ionization cross sections) of ethanol.

Ethanol is also of current interest in the field of climate physics. It is one of the most promising future sources of renewable energy that can be made from various plant materials. Owing to its lower global warming potential, this biofuel is increasingly replacing traditional fossil fuels. The growing use of ethanol as an energy carrier, however, is causing a rise in the concentration of volatile organic compounds in the Earth's atmosphere. Electron-collision-induced dissociation processes of these compounds, initiated by primary as well as secondary cosmic rays, can lead to the production of reactive species which may impact the ozone balance in the upper atmosphere. For the quantitative description of these processes, comprehensive

---

[a] e-mail: mareike.dinger@ptb.de (corresponding author)

electron interaction cross sections of ethanol are needed [2–5].

A vast number of experimental and theoretical studies on electron scattering by organic molecules have been performed to date. Surprisingly, publications describing the electron interaction cross sections of alcohol molecules are rather scarce, and most relate to electron scattering by methanol [6–18]. For the electron interaction cross sections of ethanol, only a few works have been reported. The first measurement of electron scattering cross sections was performed almost a century ago by Schmieder [6], who measured total electron scattering cross sections (TCS) of ethanol for electrons of very low energy. Some one hundred years later, Silva et al. [16] reported TCS of ethanol for electron energies between 60 and 500 eV. Differential elastic scattering cross sections (DCS) of ethanol were first published by Khakoo et al. [15], who measured the DCS for electron energies between 1 and 100 eV in the angular range of 5°–130°. They further calculated the DCS of ethanol by applying the Schwinger multichannel method and the static-exchange approximation. A few years later, Lee et al. [18] reported DCS of ethanol for electron energies between 100 eV and 1 keV in the same angular range as in the experiment by Khakoo et al. [15]. They also calculated the DCS of ethanol by describing the electron-molecule collision with a complex optical potential and solving the Lippmann–Schwinger integral equation.

In the present work, the DCS of ethanol were experimentally determined for electron energies T between 30 and 800 eV for scattering angles θ of 30° to 150° in steps of 15°. The experimental data were compared to theoretical values calculated using the modified independent atomic model (MIAM) [19] and the IAM-SCAR method [20]. Furthermore, the integral elastic cross sections (ICS) and momentum transfer cross sections (MTCS) were determined using the experimental DCS of this work and the MIAM, which was used to extrapolate the measured values.

2 Experimental procedure

The DCS of ethanol were measured using the crossed-beam arrangement. Figure 1 shows the schematic view of the experimental setup. The main components of the apparatus were a gas inlet system, an electron source, and an electron spectrometer. These were installed in an ultra-high vacuum scattering chamber, which was surrounded by three orthogonal pairs of square-shaped Helmholtz coils to compensate the external magnetic fields. The residual magnetic field was lower than 2 μT on the scattering plane. For 30 eV electrons, the orbit radius in this residual field amounts to about 9 m, which is almost 2 orders of magnitude greater than the distance between the scattering zone and the entrance aperture of the electron spectrometer. Therefore, the change of scattering angle due to the deflection of electrons by the residual magnetic field was neglected.
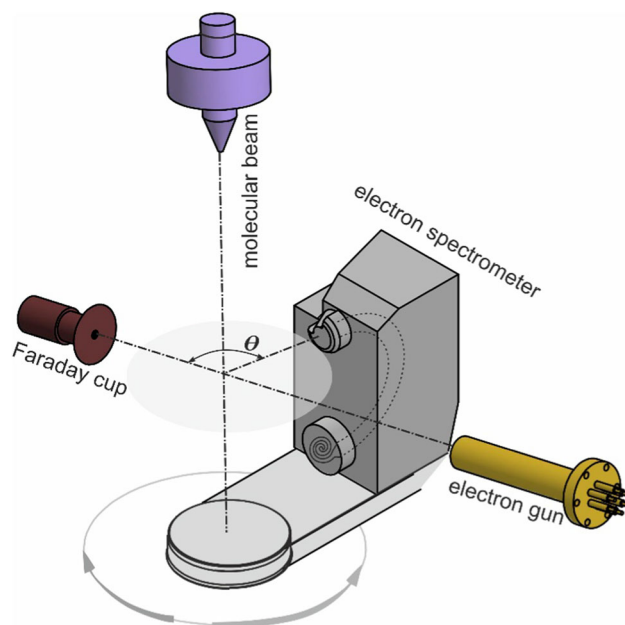
Fig. 1 Schematic view of the experimental setup used for the measurement of the DCS of ethanol. The scattering plane, defined by the symmetry axis of the electron gun and the input lens system of the electron spectrometer, is located 1.5 mm below the gas nozzle

The gas inlet system consisted of a cylindrical tube (5 mm in diameter and 12 cm in length ending in a cone shape with an exit aperture of diameter $d_a = 0.3$ mm), a needle leak valve, and a vapor (gas) reservoir with a volume of about 3.5 L. The leak valve was used to regulate the gas flow rate from the vapor reservoir to the gas effusion tube. Liquid ethanol with a purity of 99% was used as the vapor source. The flow rate of molecules through the effusion tube was adjusted by varying the driving pressure p_i at the entrance of the tube, which was monitored by means of a capacitance manometer. The reading was 2.5 mbar during the measurement of DCS. At this driving pressure, the residual pressure in the scattering chamber increased from 10^{-7} mbar to about 10^{-5} mbar.

The effusive molecular beam was crossed by an electron beam on the scattering plane located 1.5 mm below the exit aperture of the nozzle (see Fig. 1). The electron beam was generated by an electron source [21] purchased from Kimball Physics Ltd. This source provided well-focused, stable electron beams for electron energies above 30 eV with a maximal energy width of about 0.5 eV at $T = 800$ eV. In general, this energy spread reduces with decreasing electron energy. The electron current was measured by means of a Faraday cup located beyond the molecular beam and amounted to between 0.2 and 0.8 μA, depending on the electron energy. It was raised at higher energies to account for the decrease in elastic scattering events that occurs with increasing electron energy.

Electrons scattered by the molecular beam were analyzed with respect to their energy by means of an

electron spectrometer [22] fabricated by Omicron Nanotechnology GmbH. This device consists of an input lens system and a hemispherical condenser with a mean radius of 65 mm and a deflection angle of 180°. It was mounted on a turntable that enabled 360° rotation with respect to the electron source, which was installed at a fixed position. This arrangement allowed the scattering angle of the electrons to be adjusted with an angular resolution of 1°. Electrons entered the spectrometer through an aperture 1 mm in diameter and positioned 29 mm from the molecular beam axis. This corresponds to the working distance of the electron spectrometer. Three channel electron multipliers mounted at different radii behind the exit slits of the hemispherical condenser were used as detectors. The electron count rate was kept below 3×10^4/s to prevent the dependence of the detection efficiency on the count rate from becoming significant, as occurs at higher count rates. This was achieved by employing electron beam currents below $0.8\,\mu$A. The energy resolution of the electron spectrometer could be adjusted by applying different retardation voltages to the entrance aperture of the hemispherical condenser. In this work, it amounted to 1.5 eV for 800 eV electrons. It should be noted that the overall energy resolution of 1.6 eV of the apparatus is not sufficient to resolve between low-energy inelastic scattering processes such as rotational excitations and elastic scattering.

The measurement of the DCS $d\sigma_{el}/d\Omega$ of ethanol was performed using the relative flow technique [23] and N_2 as the reference gas. The determination of DCS with the relative flow technique requires the measurement of electron count rates at a given flow rate for both the gas of interest and the reference gas:

$$\frac{d\sigma_{el}}{d\Omega}(\theta, T) = \frac{d\hat{\sigma}_{el}}{d\Omega}(\theta, T) \times \frac{I}{\hat{I}} \times \frac{R}{\hat{R}} \times \frac{\hat{F}}{F}\sqrt{\frac{M}{\hat{M}}}, \quad (1)$$

where the letters with hat designate the quantities for the reference gas N_2. In Eq. (1), I is the primary electron beam current, R is the background-corrected elastic scattering rate, F is the mass flow rate, and M is the molecular mass of ethanol. The reference DCS $d\hat{\sigma}_{el}/d\Omega$ of N_2, which had been previously determined in an independent experiment, are listed in Table 1. It is noteworthy that they were measured not using the relative flow technique but absolutely by applying a different methodology, which was based on the rather accurately known DCS of He as described in detail in our earlier work [24]. The DCS of N_2 were compared to other existing experimental data [25–30] and to the theoretical database of NIST [31] to assess their quality. The latter database was considered only for electron energies above 300 eV. In general, the present data for N_2 deviated no more than 15% from the averaged values of the above external data. This deviation is taken as the uncertainty of the reference data in this work.

The application of the relative flow technique requires the same molecular beam profile for both the reference gas and the gas of interest. In the free molecular flow regime, equal gas beam profiles can be obtained if the mean free paths for intermolecular collisions in both gas beams agree [32]. This condition was met by the adjustment of the pressure p_i considering the ratio of the square of the gas kinetic diameter of both gases, which is 0.364 nm for N_2 [33] and 0.430 nm for ethanol [34]. On the one hand, an excessively high gas density in the effusion tube should be avoided so as to ensure free molecular flow conditions. On the other, a sufficiently high gas density is required to obtain the necessary number of scattering events. A satisfactory compromise was found at the driving pressure $p_i = 2.5$ mbar. At this pressure, the mean free path length λ for intermolecular collisions in ethanol vapor is 0.07 mm, giving us a Knudsen number of $Kn_d = \lambda/d_a = 0.23$. This value is slightly lower than the Knudsen number required for free molecular flow, $Kn_d > 0.3$ [35], meaning that the molecular beam was generated near the free molecular flow regime. The mass flow rates F and $\hat{F}$ were determined from the pressure fall per unit time in the gas reservoir caused by the effusion of the molecular beam. They were then employed to calculate the ratio of the number density in both molecular beams, given by the term $(\hat{F}/F) \times \sqrt{M/\hat{M}}$ in Eq. (1). This ratio was checked by measuring the attenuation of a 400 eV electron beam current after crossing each molecular beam. Using Beer's attenuation law with the TCS of ethanol [16] and N_2 [36], the number densities in the molecular beams were estimated from the measured electron current attenuation. The ratio of the number densities obtained in this way agreed with that determined from the gas flow rates within the experimental uncertainty of 15%.

The number densities in both molecular beams were small enough to fulfill the single collision condition. For instance, the flow rate of ethanol molecules at $p_i = 2.5$ mbar amounted to 3.1×10^{17}/s, which resulted in an area density of molecules of about 9×10^{12}/cm^2. Considering that the total electron scattering cross section of ethanol is lower than 10^{-14} cm^2 for electron energies above 10 eV [6, 16], the number of multiple collisions of electrons with molecules is negligibly small at this area density. In other words, the single collision condition is well satisfied.

The elastic scattering rates R and $\hat{R}$ were determined from the areas of the elastic peaks in the respective electron energy spectrum. For each electron energy and scattering angle, the same electron gun and gas inlet system operating parameters were applied to measure three electron energy spectra: the electron energy spectrum of ethanol, N_2, and the background spectrum. Apart from a few exceptions at low electron energies and small scattering angles, the signal-to-noise ratio was better than 20. Potential fluctuations of the electron beam current and gas flow rate were monitored by recording the current into the Faraday cup (see Fig. 1) as well as the pressure value p_i and the pressure in the vacuum scattering chamber.

Table 1 DCS of N_2 used as the reference cross section $d\hat{\sigma}_{el}/d\Omega$ for the relative flow technique in units of 10^{-16} cm^2/sr. The numbers in square brackets denote the powers of ten by which the preceding numbers are to be multiplied

θ/T	30 eV	40 eV	60 eV	80 eV	100 eV
30°	2.18	1.75	1.14	8.23[−1]	7.35[−1]
45°	8.58[−1]	5.83[−1]	3.28[−1]	2.42[−1]	2.16[−1]
60°	3.63[−1]	2.38[−1]	1.36[−1]	1.09[−1]	1.14[−1]
75°	1.90[−1]	1.24[−1]	7.74[−2]	7.18[−2]	8.16[−2]
90°	1.35[−1]	8.12[−2]	6.30[−2]	6.93[−2]	7.66[−2]
105°	1.78[−1]	1.09[−1]	9.76[−2]	8.92[−2]	8.24[−2]
120°	3.09[−1]	2.17[−1]	1.78[−1]	1.22[−1]	9.86[−2]
135°	4.70[−1]	3.55[−1]	2.70[−1]	1.44[−1]	1.21[−1]
150°	6.32[−1]	5.39[−1]	3.96[−1]	1.92[−1]	1.50[−1]

θ/T	200 eV	300 eV	400 eV	600 eV	800 eV
30°	3.79[−1]	3.20[−1]	3.31[−1]	2.47[−1]	2.26[−1]
45°	1.76[−1]	1.62[−1]	1.43[−1]	7.61[−2]	5.79[−2]
60°	1.07[−1]	8.26[−2]	6.02[−2]	3.94[−2]	2.56[−2]
75°	6.17[−2]	5.52[−2]	3.96[−2]	1.97[−2]	1.35[−2]
90°	4.70[−2]	4.70[−2]	2.52[−2]	1.38[−2]	8.14[−3]
105°	4.82[−2]	3.70[−2]	1.89[−2]	9.56[−3]	5.79[−3]
120°	4.94[−2]	3.24[−2]	1.71[−2]	7.65[−3]	4.41[−3]
135°	4.56[−2]	3.53[−2]	1.42[−2]	7.33[−3]	3.37[−3]
150°	4.63[−2]	3.37[−2]	1.32[−2]	6.62[−3]	2.97[−3]

3 Uncertainty analysis

The uncertainties of the experimental DCS were determined according to the *Guide to the Expression of Uncertainty in Measurement* [37]. Since the input quantities of Eq. (1) were uncorrelated, the overall standard uncertainty u_{el} of the DCS was determined from the combined variance:

$$u_{el}^2 = \sum_{i=1}^{4} \left(\frac{\partial(d\sigma_{el}/d\Omega)}{\partial x_i} \right)^2 u^2(x_i), \qquad (2)$$

where x_i stands for $d\hat{\sigma}_{el}/d\Omega$, $I/\hat{I}$, $R/\hat{R}$, and $F/\hat{F}$.

The relative uncertainty of the reference DCS, i.e., the DCS of N_2, amounts to 15% on average as explained above. Although the electron gun parameters were kept equal during the DCS measurement of ethanol and N_2, the ratio $I/\hat{I}$ varied by up to 5%. The relative uncertainty of the ratio $F/\hat{F}$, which was determined from a linear regression of the temporal pressure fall in the gas reservoir, was estimated to be 4%. These three uncertainties are of Type A. The uncertainty of $R/\hat{R}$ consists of statistical uncertainty of the background-subtracted count rates of elastically scattered electrons and of the Type B uncertainty arising due to the dependence of the detection efficiency on the count rate. Depending on the electron energy and scattering angle, the uncertainty of $R/\hat{R}$ varied from 3 to 8%. In general, this uncertainty was smaller at lower electron energies and scattering

angles. The overall uncertainty u_{el} of the experimental DCS determined using Eq. (2) amounted to about 18%.

4 Theoretical calculations

The DCS of ethanol for energies above 30 eV were calculated using two theoretical approaches, both of which are based on the independent atomic model (IAM): the modified independent atomic model (MIAM) [19] and the independent atomic model with screening-corrected additivity rule (IAM-SCAR) [20]. In the IAM, each atom within the molecule is treated as an independent scattering center, resulting in the total DCS as the sum of the individual atomic DCS. This method leads to good results at intermediate and high incident electron energies but overestimates the molecular DCS when the electron wavelength becomes comparable to the atomic separation.

The IAM-SCAR model was derived based on geometrical considerations and leads to satisfactory results even at low energies by employing screening correction factors s_i to the IAM model:

$$\frac{d\sigma_{el}^{direct}}{d\Omega} = \sum_{i}^{N} s_i^2 |f_i(\theta)|^2$$
$$+ \sum_{i \neq j}^{N} s_i s_j f_i(\theta) f_j^*(\theta) \frac{\sin(qx_{ij})}{qx_{ij}}, \qquad (3)$$

where N is the total number of atoms in the molecule, $q = 2k \sin(\theta/2)$ is the momentum transfer from the incident electron with the wavenumber k, and f_i is the scattering amplitude of the i-th atom. The second term on the right-hand side of Eq. (3) is called the molecular term and depicts the interference between two single-scattering events. It is therefore dependent on the distance x_{ij} between the two atoms involved. The screening correction factors s_i account for the reduced DCS contribution of the atoms that are in the shadow of the front atoms hit by the incident electron wave. These factors are well explained in the works of Blanco and Garcia [20, 38]. In its simplest form, Eq. (3) only considers a single interaction between the projectile and the target and, consequently, no further dispersion after the scattering event is considered. To account for multiple interactions, the contribution of redispersion is added to the above direct contribution (Eq. (3)):

$$\frac{\mathrm{d}\sigma_{\mathrm{el}}}{\mathrm{d}\Omega} = \frac{\mathrm{d}\sigma_{\mathrm{el}}^{\mathrm{direct}}}{\mathrm{d}\Omega} + \frac{\mathrm{d}\sigma_{\mathrm{el}}^{\mathrm{redispersed}}}{\mathrm{d}\Omega} + I_{\mathrm{Pol}}, \qquad (4)$$

where the formula for the redispersion term was taken from the recent publication of Blanco et al. [39]. In this latest version, called IAM-SCAR + I, Blanco et al. additionally used attenuated interference terms. The term I_{Pol} accounts for polarization effects and had to be added as f_i were calculated using atomic potentials without a correlation-polarization potential (see below)

$$I_{\mathrm{Pol}} = |f_L|^2 + 2|f_L| \sum_{i=0}^{N} |f_i| \cos(\eta_{\mathrm{L}} - \eta_i) \frac{\sin(qx_i)}{(qx_i)}. \qquad (5)$$

The distances from the center of mass to the i-th atom are denoted by x_i and the phase shifts η_{L} and η_i are related to the scattering amplitudes f_{L} and f_i via $f_{\mathrm{L}} = |f_{\mathrm{L}}|e^{i\eta_{\mathrm{L}}}$ and $f_i = |f_i|e^{i\eta_i}$, respectively, where f_{L} is the scattering amplitude due to the additional correlation-polarization potential.

The MIAM model derived by Hayashi and Kuchitsu [19] is an approach that includes intramolecular multiple-scattering events while retaining the multicenter nature of the IAM model. The approach is obtained by expanding the T matrix in a series of multiple-scattering terms and contains the contribution of the long-range correlation-polarization potential, which is essentially of a one-center nature. The contribution of the long-range correlation-polarization potential, which is identical to Eq. (5), is added to the short-range atomic potentials, leading to a differential cross section of the form:

$$\frac{\mathrm{d}\sigma_{\mathrm{el}}}{\mathrm{d}\Omega} = I_{\mathrm{Pol}} + I_{\mathrm{S}} + I_{\mathrm{SS}} + I_{\mathrm{SD}}^{(1)} + I_{\mathrm{SD}}^{(2)} + I_{\mathrm{DD}}, \qquad (6)$$

where f_{L} and f_i are, respectively, the scattering amplitudes due to the correlation-polarization potential and the atomic spherical short-range potentials.

The terms I_{S} and I_{SS} describe single-scattering and interference-of-single-scattering events, respectively, and correspond to the terms of the IAM-SCAR + I method (Eq. (3)) with $s_i = 1$. The contributions of intramolecular multiple-scattering processes are included in the terms $I_{\mathrm{SD}}^{(1)}$, $I_{\mathrm{SD}}^{(2)}$, and I_{DD}. They describe the interference between single and double scattering of the first and second kinds, and pure double scattering, respectively [19].

In this work, the scattering amplitudes f_i and f_{L} were calculated by solving the one-dimensional radial Schrödinger equation for free electrons as described in an earlier work [24]. As the atomic constituents of ethanol and tetrahydrofuran are identical, the same complex optical potentials as in Ref. [24] were employed for the determination of f_i. However, a new calculation of the correlation-polarization potential V_{cp} was necessary as the electron density distribution in ethanol is different from that in tetrahydrofuran because of their different molecular structures. For this purpose, the electron density distribution was first calculated using the quantum chemistry software GAUSSIAN09 [40] with the basis set HF/6-311G++(d,p). The molecular geometry as well as the polarizability tensor after optimization with GAUSSIAN09 can be found in Table 2. The code SCELib4 [41] was then used to obtain V_{cp} from the calculated electron density distribution. This code enables the calculation of the one-dimensional, radially dependent interaction potential using a single-center expansion. As a detailed explanation of the theory and formulae can be found in the publication of Sanna and Gianturco [42], only a short description is given here. The potential V_{cp} consists of two contributions that are dominant at different distances from the center of expansion: pure polarization effects V_{pol} at large distances, and correlation interactions V_{corr} with bound electrons within the molecule:

$$V_{\mathrm{cp}} = \begin{cases} V_{\mathrm{corr}}(\boldsymbol{r}), \ \boldsymbol{r} \leq \boldsymbol{r}_{\mathrm{c}}, \\ V_{\mathrm{pol}}(\boldsymbol{r}), \ \ \boldsymbol{r} > \boldsymbol{r}_{\mathrm{c}}, \end{cases} \qquad (7)$$

where $\boldsymbol{r}_{\mathrm{c}}$ is the second crossing point between the polarization and correlation terms and amounts to $\boldsymbol{r}_{\mathrm{c}} = 2.43874$ Å. In comparison, the distance of the C–O and C–C bond in an ethanol molecule is about 1.5 Å. The potential V_{corr} is determined using the modified free electron gas model and V_{pol} depends mainly on the static electrical properties of the molecule such as the dipole polarizabilities. The potential V_{cp} obtained in this way was averaged over all molecular orientations and then substituted into the Schrödinger equation mentioned above.

The scattering amplitudes were computed from the phase shifts of the incident electron wave using the partial-wave expansion method. Here, the calculation was truncated at a maximum angular momentum of $l = 31$. The contribution to the scattering amplitude f_i of the terms with higher angular momentum was negligibly small. For the multiple-scattering terms, i.e., the

Table 2 Molecular geometry and polarizability of ethanol (C_2H_5OH) after optimization with GAUSSIAN09. The atomic coordinates x, y and z are given in units of Å and the polarizability tensor elements α_{ij} in atomic units. The center of mass was chosen as the origin

	x	y	z		
C	1.219956	− 0.217987	− 0.000006	α_{xx}	30.669
C	− 0.090634	0.541144	0.000006	α_{xy}	− 0.142
H	1.129252	− 0.848985	0.879760	α_{yy}	27.944
H	1.292502	− 0.848981	− 0.879776	α_{xz}	0.000
H	2.057676	0.474007	− 0.000012	α_{yz}	0.000
H	− 0.152596	1.179942	− 0.879650	α_{zz}	26.432
H	− 0.152585	1.179936	0.879666		
O	− 1.142846	− 0.391127	0.000013		
H	− 1.970687	0.054153	− 0.000095		

last three terms on the right-hand side of Eq. (6), angular momenta were considered only up to $l = 31$, $l = 15$, and $l = 20$ for $I_{SD}^{(1)}$, $I_{SD}^{(2)}$, and I_{DD}, respectively.

In Fig. 2, the influence of the multiple-scattering terms within the MIAM model is illustrated by means of the examples for 100 eV and 800 eV. At 800 eV, there are almost no contributions from multiple scattering and the DCS can be well described by the single-scattering term plus a minor contribution from the molecular term I_{SS}. At this energy, the MIAM method converges toward the IAM model and the DCS can nearly be treated as the sum of the independent scattering cross sections of the atomic constituents of the molecule. The contribution from the long-range potential I_{Pol} becomes significant only at angles smaller than 10°.

At 100 eV, the highest contribution to the DCS is still given by the single-scattering term I_S, but multiple scattering can no longer be neglected. There is again a significant contribution of I_{Pol} and I_{SS} at angles smaller than 20°. Another dominant contribution in this energy regime is the interference between single and double scattering of the first kind $I_{SD}^{(1)}$, which gives an approximately constant negative contribution at angles larger than 60°. It exhibits a negative peak at around 25°, which opposes the peak in I_S appearing at this angle. The multiple-scattering terms change not only the absolute scale but also the angular dependence of DCS significantly. Multiple scattering is identified to be relevant for all angles at energies equal to or lower than 200 eV, especially in the angular range from 20° to 40°. Neglecting the multiple-scattering terms would lead to an overestimation above 20°. Moreover, a shoulder in the DCS at around 25° would be observed. The analysis further reveals that the long-range polarization potential significantly contributes to the DCS at small angles regardless of electron energy.

Strictly speaking, the theoretical approaches employed in this work are only applicable for electron energies above 50 eV [43]. Apart from the fact that the calculation of the scattering amplitude of the atoms in the molecule was based on the Born approximation, electron-molecule collision processes at low electron energies are dominated by scattering at small impact parameters. In this case, the non-spherical part of

both the short-range and long-range potentials may play a significant role in elastic scattering and must therefore be considered. Therefore, the theoretical DCS of ethanol for 30 eV and 40 eV are much less reliable than for those above 50 eV.

5 Results and discussion

The measured DCS of ethanol in the range of 30–800 eV are listed in Table 3 and compared to the published values of Khakoo et al. [15] and Lee et al. [18] in Figs. 3 and 4. As expected, they show angular dependence similar to that of the DCS of other gases. For energies above 300 eV, the measured DCS generally decrease at higher scattering angles, whereas they converge against a constant value at high scattering angles in the case of $T = 200$ eV. For $T < 200$ eV, a minimum at around 90° is observed in the DCS. This angular dependence is in accordance with the predictions of existing theoretical approaches such as the MIAM [19] and Lippmann–Schwinger methods [18].

The results of this work agree reasonably well with those of Khakoo et al. [15] and Lee et al. [18] within the stated experimental uncertainty. At electron energies of $T \geq 100$ eV, the agreement is generally very good, with the exception that the presence of a small shoulder indicated by the data of Lee et al. [18] in the angular range between 40° and 80° at $T = 100$ eV could not be confirmed by the current results. To uniquely verify the presence of this shoulder, the DCS with lower experimental uncertainty are required. At $T = 30$ eV, there is only poor agreement between the present results and the data of Khakoo et al. [15], but the deviations are still within the 3-sigma range of uncertainty. Here, the data of Khakoo et al. [15] likewise show a weak shoulder at scattering angles between 40° and 70°, which is again not reproduced by the present results. No comparison with the experimental results of Lee et al. [18] is possible at this energy range, since they performed the measurements for electron energies higher than 100 eV.

As can be seen from Figs. 3 and 4, the data calculated using the IAM-SCAR + I and MIAM reproduce the experimental results over the entire energy range

Fig. 2 Relative contributions $I_i / \sum_j I_j$ of the different terms I_i in the MIAM model as a function of the scattering angle θ for the energies **a** 100 eV and **b** 800 eV. The terms $I_{SD}^{(2)}$ and I_{DD} are at least an order of magnitude smaller than the other terms and are therefore not shown in this figure
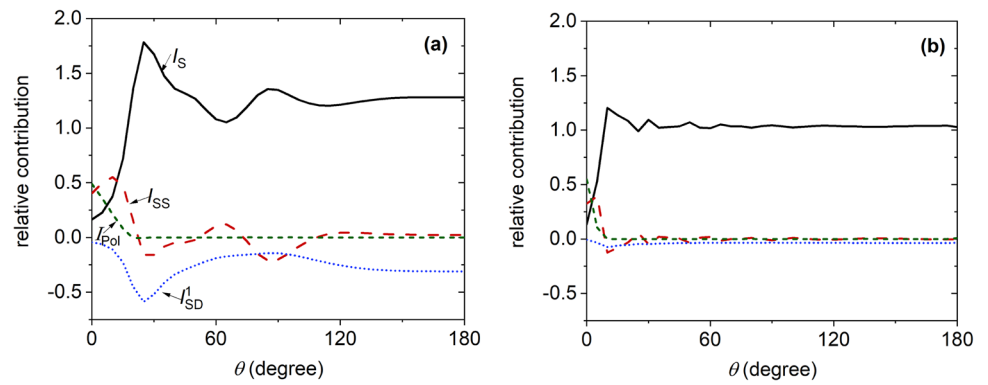

Table 3 DCS of ethanol as a function of the scattering angle θ for different electron energies T in units of 10^{-16} cm^2/sr. The DCS for $\theta \leq 25°$ and $\theta \geq 155°$, given in italic numbers, were obtained by the extrapolation of the present experimental results using the MIAM. Integral elastic cross sections (ICS) σ_{el} and momentum transfer cross sections (MTCS) σ_m are given in units of 10^{-16} cm^2. The numbers in square brackets denote the powers of ten by which the preceding numbers are to be multiplied

θ/T	30 eV	40 eV	60 eV	80 eV	100 eV
0°			*1.27[+ 2]*	*1.27[+ 2]*	*1.13[+ 2]*
5°			*8.90[+ 1]*	*8.29[+ 1]*	*7.32[+ 1]*
10°			*4.97[+ 1]*	*4.10[+ 1]*	*3.26[+ 1]*
15°			*2.24[+ 1]*	*1.57[+ 1]*	*1.08[+ 1]*
20°			*8.15*	*5.08*	*3.39*
25°			*2.73*	*1.92*	*1.53*
30°	1.85	2.11	1.56	1.31	1.01
45°	1.03	7.68[− 1]	4.87[− 1]	3.99[− 1]	3.27[− 1]
60°	6.09[− 1]	3.25[− 1]	2.32[− 1]	1.85[− 1]	1.73[− 1]
75°	3.14[− 1]	1.88[− 1]	1.33[− 1]	1.25[− 1]	1.14[− 1]
90°	1.87[− 1]	1.24[− 1]	9.18[− 2]	1.09[− 1]	9.64[− 2]
105°	2.34[− 1]	1.35[− 1]	1.34[− 1]	1.42[− 1]	1.14[− 1]
120°	4.03[− 1]	1.87[− 1]	2.30[− 1]	2.03[− 1]	1.37[− 1]
135°	5.86[− 1]	2.91[− 1]	3.46[− 1]	2.30[− 1]	1.70[− 1]
150°	9.02[− 1]	4.49[− 1]	5.59[− 1]	3.29[− 1]	2.26[− 1]
155°			*5.54[− 1]*	*3.83[− 1]*	*2.43[− 1]*
160°			*5.98[− 1]*	*4.07[− 1]*	*2.55[− 1]*
165°			*6.34[− 1]*	*4.25[− 1]*	*2.64[− 1]*
170°			*6.61[− 1]*	*4.39[− 1]*	*2.71[− 1]*
175°			*6.78[− 1]*	*4.48[− 1]*	*2.76[− 1]*
180°			*6.84[− 1]*	*4.50[− 1]*	*2.77[− 1]*
σ_{el}			1.81[+ 1]	1.46[+ 1]	1.15[+ 1]
σ_m			3.94	3.01	2.23

θ/T	200 eV	300 eV	400 eV	600 eV	800 eV
0°	*1.16[+ 2]*	*1.24[+ 2]*	*1.16[+ 2]*	*1.33[+ 2]*	*1.67[+ 2]*
5°	*5.50[+ 1]*	*4.66[+ 1]*	*3.99[+ 1]*	*3.35[+ 1]*	*2.79[+ 1]*
10°	*1.52[+ 1]*	*9.48*	*7.07*	*5.61*	*4.95*
15°	*3.98*	*2.95*	*2.63*	*2.47*	*2.16*
20°	*1.83*	*1.60*	*1.40*	*1.15*	*9.98[− 1]*
25°	*1.12*	*9.03*	*7.44[− 1]*	*6.76[− 1]*	*5.64[− 1]*
30°	6.94[− 1]	5.57[− 1]	4.15[− 1]	3.38[− 1]	3.19[− 1]
45°	1.89[− 1]	1.58[− 1]	1.59[− 1]	1.07[− 1]	8.08[− 2]
60°	1.12[− 1]	8.61[− 2]	6.84[− 2]	5.57[− 2]	3.65[− 2]
75°	7.00[− 2]	5.44[− 2]	4.10[− 2]	2.91[− 2]	1.80[− 2]

Table 3 (continued)

θ/T	200 eV	300 eV	400 eV	600 eV	800 eV
90°	5.76[−2]	3.50[−2]	2.60[−2]	2.20[−2]	1.24[−2]
105°	6.00[−2]	3.70[−2]	1.95[−2]	1.39[−2]	8.48[−3]
120°	6.21[−2]	3.09[−2]	1.63[−2]	1.15[−2]	5.88[−3]
135°	6.77[−2]	3.74[−2]	1.85[−2]	1.08[−2]	5.24[−3]
150°	6.24[−2]	3.61[−2]	1.52[−2]	9.60[−3]	4.33[−3]
155°	*6.41[−2]*	*2.89[−2]*	*1.61[−2]*	*8.01[−3]*	*4.85[−3]*
160°	*6.48[−2]*	*2.88[−2]*	*1.59[−2]*	*7.71[−3]*	*4.57[−3]*
165°	*6.54[−2]*	*2.87[−2]*	*1.58[−2]*	*7.69[−3]*	*4.57[−3]*
170°	*6.58[−2]*	*2.87[−2]*	*1.57[−2]*	*7.59[−3]*	*4.49[−3]*
175°	*6.60[−2]*	*2.86[−2]*	*1.56[−2]*	*7.50[−3]*	*4.36[−3]*
180°	*6.61[−2]*	*2.88[−2]*	*1.60[−2]*	*8.19[−3]*	*5.00[−3]*
σ_{el}	6.55	5.00	4.10	3.39	2.83
σ_m	1.01	6.43[−1]	4.34[−1]	3.19[−1]	2.16[−1]
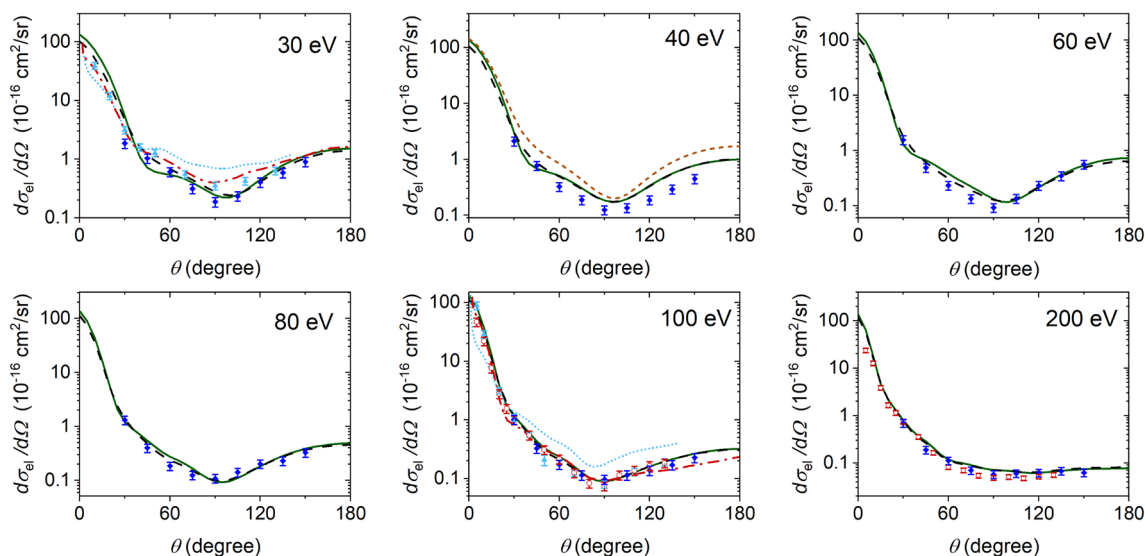
Fig. 3 DCS of ethanol measured in the present work (filled diamond) for the energies 30 eV to 200 eV in comparison to the results of Khakoo et al. (filled triangle) [15] and Lee et al. (circle) [18]. The theoretical values calculated using the MIAM and IAM-SCAR + I are displayed as solid and dashed lines, respectively, and the theoretical calculations from Khakoo et al. [15] and Lee et al. [18] for 30 eV and 100 eV as dotted and dashed dotted lines. For comparison, the basic IAM model with additional polarization effects is included for 40 eV as a short-dashed line

rather accurately. At energies above 80 eV, satisfactory agreement between IAM-SCAR + I, MIAM and the experimental DCS within the experimental uncertainties is achieved. Furthermore, the theoretical values in this energy range reproduce the experimental results of this work better than those of other groups. Exceptionally, the IAM-SCAR + I and MIAM results at T = 100 eV agree better with the data of Lee et al. [18] than with those of this work. At energies $T \leq$ 80 eV, there is relatively poor agreement between theoretical results and the present experimental values. In this energy range, the theoretical values are in general higher than the experimental data, but the agreement between both improves with increasing energy. In

addition, a significant deviation is found in the angular range from 40° to 80°, where a shoulder is observed in the theoretical DCS but not in the present experimental data. This deviation is particularly pronounced at the energies 30 eV and 40 eV in the theoretical values from MIAM, whereas the IAM-SCAR + I decreases rather smoothly until reaching the minimum at about 90°. For comparison, the basic IAM model, which includes single scattering (I_S), interference between single scattering events (I_{SS}) and polarization (I_{Pol}), is included in Fig. 3 for the energy 40 eV. It is worthwhile mentioning that the shoulder observed in MIAM arises mainly from single scattering I_S and the interference between single and double scattering of the first kind $I_{SD}^{(1)}$.
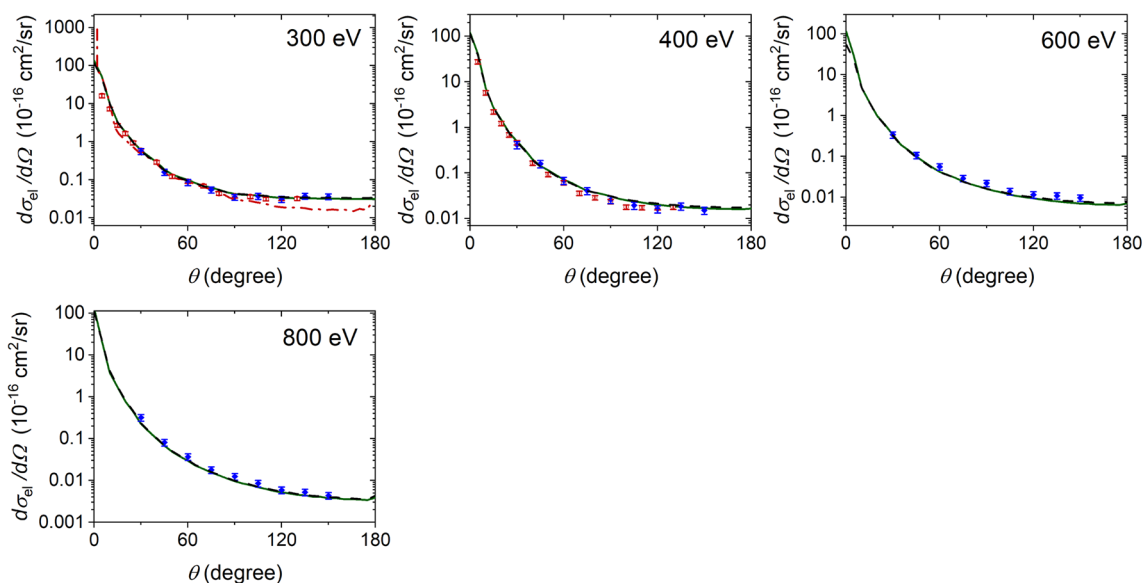
Fig. 4 Same as in Fig. 3 but for the energies 300 eV to 800 eV

It is evident from Fig. 2 that the influence of multiple scattering terms increases with decreasing energy. As described above, the IAM-SCAR + I and MIAM are of limited validity for $T < 50$ eV. Therefore, it is not surprising that there is only poor agreement between experimental and theoretical data at the energies 30 eV and 40 eV. Nevertheless, the differences between both datasets are still on the order of the experimental uncertainty. It should be noted that the term $I_{SD}^{(2)}$ has been disregarded for the electron energies 30 eV and 40 eV as it was subject to high numerical instabilities, especially due to oscillations occurring in spherical Bessel functions.

When comparing the theoretical results of this work to those of Lee et al. [18], better agreement with the existing experimental data is achieved with the IAM-SCAR + I and MIAM for energies $T \geq 100$ eV, while the model used by Lee et al. [18] better complies with experimental values below 100 eV. This is probably to be attributed to the fact that the interaction potentials employed by Lee et al. [18] are more suitable for the description of the scattering of low-energy electrons. Moreover, the theoretical results of Lee et al. [18] reproduce the experimental data better than do those of Khakoo et al. [15], who did not consider absorption effects [18].

Figure 5 shows integral elastic cross sections (ICS) and momentum transfer cross sections (MTCS) of ethanol. They were determined by the integration of $d\sigma_{el}/d\Omega$ and $(1 - \cos\theta)d\sigma_{el}/d\Omega$, respectively, over the solid angle. The DCS outside the measured angular range were estimated by extrapolating the experimental data using the MIAM. As can be seen from Fig. 5, the results of this work agree well with those of Khakoo et al. [15] and Lee et al. [18] within the uncertainty. As

the MIAM method used for the extrapolation is of limited validity for energies $T \leq 50$ eV, no ICS and MTCS were calculated for 30 eV and 40 eV. The uncertainties of the ICS and MTCS amounted to 23%. They were obtained from the estimated uncertainty of the extrapolation used to obtain the DCS for the scattering angles $\theta < 30°$ and $\theta > 150°$, and from the uncertainties of the experimental DCS. It should be noted that due to the limited angular range, the present experimental data contributed to only about 20% of the determined ICS. Therefore, the ICS values of this work are prone to the inaccuracy of the theoretical models. Considering, however, that the MIAM reproduces the experimental data of Khakoo et al. [15] and Lee et al. [18] well down to scattering angles of 5° above 50 eV within the stated experimental uncertainties, the calculation of the ICS using the extrapolated DCS is feasible.

Finally, it should be noted that the DCS of the present work include the cross sections of low-energy inelastic channels such as rotational excitations because of finite instrumental energy resolution as mentioned above. While the induced polarization effect considered in the IAM-SCAR + I and MIAM enhances the elastic scattering at small angles, permanent dipole moments lead to rotational excitations. As the ethanol molecule has a considerable permanent dipole moment of 1.68 D [44], the upper limit of the contamination of the DCS of ethanol by rotational excitation cross sections was estimated using the formula of Collins and Norcross [45]. The calculation showed that the contamination does not exceed 10%, which is lower than the experimental uncertainties of the present data. The magnitude of the contamination decreases with increasing scattering angle.

Fig. 5 a ICS and **b** MTCS of this work (filled diamond) compared to the results of other groups: (filled triangle) Khakoo et al. [15], (circle) Lee et al. [18]
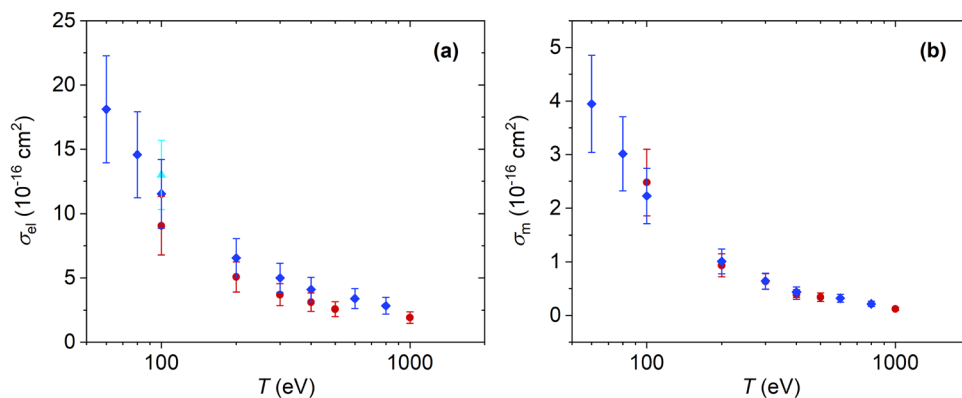
6 Conclusion

The elastic scattering of electrons by ethanol was comprehensively studied in this work both experimentally and theoretically. A comparison of the experimental results of this work to those available in literature, i.e., the data of Khakoo et al. [15] and Lee et al. [18], showed good agreement over the entire energy and angular range within the experimental uncertainty. The theoretical values obtained by the IAM-SCAR + I and MIAM approaches align reasonably well with the experimental DCS at energies $T > 80$ eV.

The comparison of the theoretical values to the existing experimental data reveals that the MIAM and IAM-SCAR + I predict the DCS of small molecules with sufficient accuracy for electron energies $T \geq 80$ eV. In general, both models reproduce the experimental data with the same accuracy, especially for $T \geq 100$ eV. This means that the screening introduced in the IAM-SCAR + I combined with the interference and redispersion terms can successfully reproduce multiple scattering events, which are considered in the MIAM. At electron energies around and below 50 eV, the quality of the IAM-SCAR + I and MIAM suffers from the model inherent approximations. Here, ab initio calculation with a more realistic interaction potential, is required. Nevertheless, in consideration of the wide spread of experimental values at 30 eV, more experimental data at low energies are needed to make a reliable statement about the eligibility of both IAM based models at low energies.

Finally, the ICS and MTCS of ethanol obtained on the basis of the experimental DCS of this work and the extrapolated values using the MIAM agree well with the results of other groups within the experimental uncertainty.

Author contributions

The majority of the work was done by MD, who supported the experiment by performing data analysis, carried out theoretical calculations, and wrote a great part of the original draft of the manuscript. YP performed the measurements. PH and WYB were involved in setting up and conducting the experiment. WYB supervised the work. All authors reviewed and edited the manuscript.

Data Availability Statement This manuscript has no associated data or the data will not be deposited [Authors' comment: The authors confirm that all scientifically relevant final data are present in the paper. Additional raw data are available from the corresponding author upon reasonable request.]

References

1. S.F. Kry, J. Lye, C.H. Clark, N. Andratschke, A. Dimitriadis, D. Followil, R. Howell, M. Hussein, M. Ishikawa, S. Kito, T. Kron, J. Lee, J. Michalski, A.F. Monti, N. Reynaert, P. Taylor, K. Venables, Y. Xiao, J. Lehmann, Radiother Oncol. **159**, 106 (2021)

2. R.L. Tanner, A.H. Miguel, J.B. De Andrade, J.S. Gaffney, G.E. Streit, Environ. Sci. Technol. (1988). https://doi.org/10.1021/es00174a005

3. A. Salvo, F.M. Geiger, Nat. Geosci. **7**, 6 (2014)

4. R.E. Dunmore, L.K. Whalley, T. Sherwen, M.J. Evans, D.E. Heard, J.R. Hopkins, J.D. Lee, A.C. Lewis, R.T. Lidster, A.R. Rickard, J.F. Hamilton, Faraday Discuss. **189**, 105–120 (2016)

5. J.D. Wiley, G.B. Avery, J.D. Felix, R.J. Kieber, R.N. Mead, M.S. Shimizu, N.P.J. Clim, Atmos. Sci. **2**, 3 (2019)

6. F. Schmieder, Z. Elektrochem, Angew. Phys. Chem. **36**, 700 (1930)

7. S. Mori, Y. Katayama, O. Sueoka, At. Coll. Res. Jpn. Prog. Rep. **11**, 19 (1985)

8. N. Durić, I. Cadez, M. Kurepa, Fizika (Zagreb) **21**, 339 (1989)

9. C. Szmytkowski, A.M. Krzysztofowicz, J. Phys. B **28**, 4291 (1995)

10. S.K. Srivastava, E. Krishnakumar, A.F. Fucaloro, T. van Note, J. Geophys. Res. **101**, 26155 (1996)

11. K.N. Joshipura, M. Vinodkumar, Eur. Phys. J. D **5**, 229–235 (1999)

12. R. Rejoub, C.D. Morton, B.G. Lindsay, R.F. Stebbings, J. Chem. Phys. **118**, 1756 (2003)

13. D. Bouchiha, J.D. Gorfinkiel, L.G. Caron, L. Sanche, J. Phys. B **40**, 1259 (2007)

14. M. Vinodkumar, C. Limbachiya, K.N. Joshipura, B. Vaishnav, S. Gangopadhyay, J. Phys.: Conf. Ser. **115**, 012013 (2008)

15. M.A. Khakoo, J. Blumer, K. Keane, C. Campbell, H. Silva, M.C.A. Lopes, C. Winstead, V. McKoy, R.F. da Costa, L.G. Ferreira, M.A.P. Lima, M.H.F. Bettega, Phys. Rev. A **77**, 042705 (2008)

16. D.G.M. Silva, T. Tejo, J. Muse, D. Romero, M.A. Khakoo, M.C.A. Lopes, J. Phys. B **43**, 015201 (2010)

17. R.T. Sugohara, M.G.P. Homem, I.P. Sanches, A.F. de Moura, M.T. Lee, I. Iga, Phys. Rev. A **83**, 032708 (2011)

18. M.-T. Lee, G.L.C. de Souza, L.E. Machado, L.M. Brescansin, A.S. dos Santos, R.R. Lucchese, R.T. Sugohara, M.G.P. Homem, I.P. Sanches, I. Iga, J. Chem. Phys. **136**, 114311 (2012)

19. S. Hayashi, K. Kuchitsu, J. Phys. Soc. Jpn. **41**, 1724 (1976)

20. F. Blanco, G. Garcia, Phys. Lett. A. **330**, 230 (2004)

21. Electron Gun ELG-2A, Kimball Physics Inc, Wilton, NH.

22. AR 65 Energy Analyzer, Scienta Omicron GmbH, Taunusstein, Germany

23. S.K. Srivastava, A. Chutjian, S. Trajmar, J. Chem. Phys. **63**, 2659 (1975)

24. W.Y. Baek, M. Bug, H. Rabus, E. Gargioni, B. Grosswendt, Phys. Rev. A **86**, 032702 (2012)

25. J.P. Bromberg, J. Chem. Phys. **52**, 1243 (1970)

26. R.H.J. Jansen, F.J. De Heer, H.J. Luyken, B. Van Wingerden, H.J. Blaauw, J. Phys. B: Atom. Mol. Phys. **9**, 185 (1976)

27. R.D. DuBois, M.E. Rudd, J. Phys. B: Atom. Mol. Phys. **9**, 2657 (1976)

28. S.K. Srivastava, A. Chutjian, S. Trajmar, J. Chem. Phys. **64**, 1340 (1976)

29. T.W. Shyn, G.R. Carignan, Phys. Rev. A. **22**, 923 (1980)

30. J.C. Nickel, C. Mott, I. Kanik, D.C. McCollum, J. Phys. B: Atom. Mol. Opt. Phys. **21**, 1867 (1988)

31. A. Jablonski, F. Salvat, C. J. Powell, and A. Y. Lee, NIST Electron Elastic-Scattering Cross-Section Database Version 4.0, NIST Standard Reference Database Number 64, National Institute of Standards and Technology, Gaithersburg MD, 20899 (2016).

32. J.C. Nickel, P.W. Zetner, G. Shen, S. Trajmar, J. Phys. E: J. Sci. Instrum. **22**, 730 (1989)

33. N. Mehio, S. Dai, D.-E. Jiang, J. Phys. Chem. A **118**(6), 1150 (2014)

34. Y. Tang, D. Dubbeldam, S. Tanase, A.C.S. Appl, Mater. Interfaces **11**, 41383 (2019)

35. V. Schmidt, *Electron Spectrometry of Atoms using Synchrotron Radiation*, vol. 6 (Cambridge University Press, Cambridge, 1997)

36. Y. Itikawa, J. Phys. Chem. Ref. Data **35**, 31 (2006)

37. International Organization for Standardization (ISO), Guide to the Expression of Uncertainty in Measurement (ISO, Geneva, 1993)

38. F. Blanco, G. Garcia, Phys. Lett. A **317**, 458 (2003)

39. F. Blanco, L. Ellis-Gibbings, G. Garcia, Chem. Phys. Lett. **645**, 71 (2016)

40. GAUSSIAN 09, Gaussian, Inc., Wallingford, CT.

41. N. Sanna, G. Morelli, S. Orlandini, M. Tacconi, I. Baccarelli, Comput. Phys. Commun. **248**, 106970 (2020)

42. N. Sanna, F.A. Gianturco, Comput. Phys. Commun. **128**, 139 (2000)

43. F. Salvat, A. Jablonski, C.J. Powell, Comput. Phys. Commun. **165**, 157 (2005)

44. R.K. Katar, C.R. Quade, J. Chem. Phys. **72**, 4300 (1980)

45. L.A. Collins, D.W. Nocross, Phys. Rev. A **18**, 467 (1978)